INL/JOU-17-41043-Revision-0

Thermal Predictions of the AGR-3/4 Experiment Using PIE-Measured Time Varying Gas Gaps

Grant L. Hawkes, James W. Sterbentz, John T. Maki

November 2016

The INL is a U.S. Department of Energy National Laboratory
operated by Battelle Energy Alliance

INL/JOU-17-41043-Revision-0

Thermal Predictions of the AGR-3/4 Experiment Using PIE-Measured Time Varying Gas Gaps

Grant L. Hawkes, James W. Sterbentz, John T. Maki

November 2016

Idaho National Laboratory
Idaho Falls, Idaho 83415

http://www.inl.gov

Prepared for the
U.S. Department of Energy

Under DOE Idaho Operations Office
Contract DE-AC07-05ID14517

`Thermal Predictions of the AGR-3/4 Experiment with PIE Measured Time Varying Gas Gaps

Grant L. Hawkes[1]
Idaho National Laboratory
2525 Fremont, MS 3870, Idaho Falls, ID 83415
Grant.Hawkes@inl.gov

James W. Sterbentz
Idaho National Laboratory
2525 Fremont, MS 3870, Idaho Falls, ID 83415
James.Sterbentz@inl.gov

John T. Maki
Idaho National Laboratory
2525 Fremont, MS 3870, Idaho Falls, ID 83415
John.Maki@inl.gov

Binh T. Pham
Idaho National Laboratory
2525 Fremont, MS 3818, Idaho Falls, ID 83415
Binh.Pham@inl.gov

ABSTRACT

A thermal analysis was performed for the Advanced Gas Reactor test experiment (AGR-3/4) with post irradiation examination (PIE) measured time (fast neutron fluence) varying gas gaps. The experiment was irradiated at the Advanced Test Reactor (ATR) at the Idaho National Laboratory. Several fuel irradiation experiments are planned for the AGR Fuel Development and Qualification Program, which supports the development of the Very-High-Temperature gas-cooled Reactor under the Advanced Reactor Technologies project.

[1] Corresponding author.

The AGR-3/4 test was designed primarily to assess fission product transport through various graphite materials. Irradiation in the ATR started in December 2011 and finished in April 2014. Forty-eight (48) tristructural-isotropic fueled compacts were inserted into 12 separate capsules for the experiment. The purpose of this analysis was to calculate the temperatures of each compact and graphite layer to obtain daily average temperatures using PIE-measured time (fast neutron fluence) varying gas gaps and compare with experimentally measured thermocouple data. PIE-measured experimental data was used for the graphite shrinkage versus fast neutron fluence. PIE dimensional measurements were taken on all fuel compacts, graphite holders, and all of the graphite rings used. Heat rates were input from a detailed physics analysis for each day during the experiment. Individual heat rates for each non-fuel component were input as well. A steady-state thermal analysis was performed for each daily calculation. A finite element model was created for each capsule.

INTRODUCTION

The Advanced Gas Reactor (AGR) experiments AGR-1 and AGR-2 irradiated in the Advanced Test Reactor (ATR) have previously been modeled for daily thermal evaluation by the Hawkes et al noted in [1] and [2]. The author discusses in these references similar topics to this article, such as variable gas gaps, mesh sensitivity, thermal conductivity varying with fast neutron fluence, and daily thermal heat rates imported from physics analysis using the Monte Carlo N-Particle (MCNP) code. These first two experiments were shake-down tests for the tristructural-isotropic (TRISO) fuel particles in compacts.

The AGR-3/4 experiment was placed in the northeast flux trap position in the ATR core, as shown in Fig. 1. The AGR-3/4 experiment is comprised of 12 individual capsules, approximately 0.07 m (2.75 in) diameter by 0.10 m (4.0 in) tall, stacked on top of each other to form the 1.219 m (48.0 in) tall test train. Each capsule contains four

TRISO-particle compacts that are approximately 0.0127 m (0.5 in) diameter by 0.0127 m (0.5 in) long. The compacts are composed of TRISO fuel particles bound together by a carbon matrix. Each compact contains 1890 fissile particles with 20 designed-to-fail particles (36 vol% particle packing fraction, 64% graphite powder in a carbon resin). Each fuel particle is comprised of a 350×10^{-6} m diameter oxycarbide kernel with 19.75% U-235. Subsequent outer layers are comprised of a 100×10^{-6} m porous carbon buffer layer, 40×10^{-6} m low-density pyro-carbon layer, 35×10^{-6} m SiC layer, with the outside being a high-density 40×10^{-6} m pyro-carbon layer. Each capsule, as shown in Fig. 2, is supplied with a flowing helium/neon gas mixture to control the test temperature and sweep any fission gases that are released to the fission product monitoring system. Temperature control is accomplished by adjusting the gas mixture ratio of the two gases (helium and neon) with differing thermal conductivities in the gas gaps.

Previous papers by the author discussing the thermal model of the AGR-3/4 experiment were presented in 2013 and 2014. The first paper [3] discusses a general overview of the thermal model with a small portion of the daily calculations reported. The second paper [4] shows daily thermal predictions with time (fast neutron fluence) varying gas gaps. The gas gaps are calculated from other experiments and sources. Unique to this current article are the actual post-irradiation examination (PIE) measured gas gaps from the AGR-3/4 experiment and incorporated into the thermal model.

An axial view of two of the 12 capsules is shown in Fig. 2. Four through tubes carry thermocouples (TC) and gas lines to each individual capsule. All 12 capsules have

their own gas mixture and fission product gas return line. Each capsule has a fuel compact in the center surrounded by three graphitic annuli, as shown in Fig. 3. Gap numbers are also noted in Fig. 3. Symmetry may not be assumed as the heat rates vary azimuthally for each graphite layer. The graphite annuli proceeding from the compact out are: matrix ring (inside), graphite ring, and graphite sink (outside). As-built dimensions for each layer are shown in Table 1. Gas gaps near the axial core center where more heat is generated are smaller, while gas gaps on the top and bottom of the experiment train are larger. Gas gaps for the two inner most gaps are very small and not perceptible in Fig. 3. Each of these four components is designed to operate at a specified temperature in all 12 capsules. As-built dimensions for the four temperature control gas gaps separate these components and are shown in Table 2. There are a total of 48 gas gaps in the entire test train. Reactor water flows on the outside of the stainless steel capsule shell. A cutaway rendering of a typical capsule is shown in Fig. 4. One of the main goals of this experiment was to make the bulk of the heat from the compacts flow radially out of the capsule instead of axially out the ends of the capsule. Zirconia, grafoil, and graphite felt insulators are placed on the top and bottom of each capsule shown in Fig. 4.

The Abaqus [5] model has a direct volume-for-volume correlation with the physics model. A similar physics model is discussed in Sterbentz et al.'s 2010 paper [6] for the heating of the compacts (each compact is evenly axially divided into two equal parts). The goal of these predictions is to be able to adjust the TC set points as the fuel burns during the experiment to maintain constant fuel or graphite layer temperature.

NUMERICAL MODEL AND DISCUSSION

The finite element mesh with a cutaway view colored by different materials of the entire model is shown in Fig. 5. A Cartesian coordinate system is appropriate for this model because of the three-dimensionality of the heat flow. Approximately 400,000 eight-noded hexahedral brick elements (DC3D8) were exclusively used in all 12 capsule models. Several mesh convergence studies [7] have been performed on the mesh. Identical agreement for this mesh and a mesh with twice as many elements in each direction was obtained. The gap conductance model was implemented for the outside three gas gaps, while the inner-most gas gap had hexagonal brick elements. This inner-most gap was modeled with brick elements since all the capsules had the same gas gap. Since only one basic mesh was created and propagated to the other 11 capsules, various gas gap conductivities and gap conductances were implemented by taking into account each individual gap dimension. The top and bottom of each model were assumed to be adiabatic. This implies that we are ignoring radiation heat transfer from the top of one capsule to the bottom of the one above. The gas gap between capsules is more than 0.0127 m (0.5 in).

The fuel compact thermal conductivity was taken from correlations presented by Gontard and Nabielek [8] which gives correlations for conductivity, taking into account temperature, temperature of heat treatment, neutron fluence, and TRISO-coated particle packing fraction (where packing fraction is defined as the total volume of particles divided by the total volume of the compact).

In this work, the convention used to quantify neutron damage to a material is neutron fast fluence, (n/m^2, E_n *>0.18 MeV*) where E_n is the neutron energy with units of MeV, yet in the work by Gontard, the unit used was the dido nickel equivalent (DNE). In order to convert from the DNE convention to the fast fluence > 0.18 MeV, the following conversion [9] was used:

$$\Gamma_{>0.18MeV} = 1.52\Gamma_{DNE} \quad (1)$$

where Γ is neutron fluence in either the > 0.18 MeV unit or *DNE*. The correlations in the report by Gontard were further adjusted to account for differences in fuel compact density. The correlations were developed for a fuel compact matrix density of 1750 kg/m^3, whereas the compact matrix used in AGR-3/4 had a density of approximately 1600 kg/m^3. The thermal conductivities were scaled according to the ratio of densities (0.91) in order to correct for this difference.

Fig. 6 shows a three-dimensional plot of the fuel compact thermal conductivity varying with fast neutron fluence and temperature using the Chiew & Gland correlation [10] for particles in a matrix described as:

$$\frac{k_e}{k_m} = \frac{1+2\beta\varphi+(2\beta^3-0.1\beta)\varphi^2+0.05\varphi^3 e^{4.5\beta}}{1-\beta\varphi} \quad (2)$$

$$where\ \beta = \frac{\kappa-1}{\kappa+2}\ \ and\ \kappa = \frac{k_p}{k_m}$$

where k_e is the effective thermal conductivity, k_m is the matrix thermal conductivity, k_p is the particle thermal conductivity, and ϕ is the particle packing fraction.

For fluences greater than 1.0×10^{25} neutrons/m^2 ($E_n > 0.18$ MeV), the conductivity increases as fluence increases for higher temperatures because of the annealing of radiation-induced defects in the material with high temperatures, while the opposite occurs at lower temperatures.

The thermal conductivity of the matrix ring was taken from the fuel compacts correlation with a fuel particle packing fraction of zero. This was done since a pure matrix material conductivity was not available. A plot similar in shape to the fuel compacts, with higher conductivity is shown in Fig. 7.

Two types of nuclear grade graphite were used in this experiment: PCEA and IG-110. The unirradiated thermal conductivity of these two types of graphite were conducted at the Idaho National Laboratory (INL) and discussed in Windes's 2012 report [11]. The effect of irradiation on the thermal conductivity of the graphite was accounted for in the analysis using the following emprical correlation by Snead [12].

$$\frac{k_{irr}}{k_0} = (0.00017T_{irr} - 0.25)log(dpa) + 0.000683T_{irr} \quad (3)$$

where k_{irr} and k_0 are the thermal conductivities of irradiated and unirradiated graphite, respectively, T_{irr} is the irradiation temperature (°C), and *dpa* is the number of carbon atom displacements per atom from fast neutrons. The multiplier used to convert

fast fluence (>0.18 MeV) to dpa is 8.23×10^{-26} dpa/(n/m^2) and comes from Sterbentz [13]. Typical values for PCEA and IG-110 unirradiated graphite (k_0) are 131 and 90 W/m K respectively at 300°C and slope down to 58 and 47 (same units) at 1200°C. Fig. 8 shows a three-dimensional plot of this ratio (k_{irr}/k_o) varying with dpa and temperature. This ratio of irradiated to unirradiated thermal conductivity increases for higher temperatures and decreases for higher dpa.

Fig. 9 shows a plot of the helium/neon sweep gas thermal conductivity versus temperature and mole fraction of helium. The thermal conductivity increases as the helium mole fraction increases and as the temperature increases. Heat produced in the fuel compacts and graphite components is transferred through the gas gaps surrounding the compacts and components via a gap conductance model using the gap width and the conductivity of the sweep gas as discussed below. Both radiation and conduction heat transfer were considered across every gap. However, because the thermal capacitance of the sweep gas is very low (5.0×10^{-7} m^3/s), advection is not considered in the sweep gas. The sweep gas is modeled as being stationary. The convective heat transfer from these sweep gases would be less than 0.01% of the heat transfer across the gap because of the low density, low flow rate, and low thermal capacitance. The thermal conductivity of the sweep gas mixture was determined using a set of correlations from Brown University [14] for mixtures of Noble gases.

The governing equation for steady-state heat transfer in the model is:

$$0 = \frac{\partial}{\partial x}\left(k(T)\frac{\partial T}{\partial x}\right) + \frac{\partial}{\partial y}\left(k(T)\frac{\partial T}{\partial y}\right) + \frac{\partial}{\partial z}\left(k(T)\frac{\partial T}{\partial z}\right) + \dot{q} \quad (4)$$

where *T* is temperature, *x, y*, and *z* are Cartesian coordinate directions, *k(T)* is the thermal conductivity varying with temperature, and *q* is the heat source. Approximately 80-85% of the heat transfer across the gas gaps is by conduction, 15-20% by radiation across the control gas gap, and with less than 0.01% by advection. Ranges are given here to cover different temperatures for the fuel compacts.

The governing equation for radiation heat transfer across the gas gaps is:

$$q_{net} = \frac{\sigma\left(T_1^4 - T_2^4\right)}{\frac{(1-\varepsilon_1)}{\varepsilon_1 A_1} + \frac{1}{A_1 F_{12}} + \frac{(1-\varepsilon_2)}{\varepsilon_2 A_2}} \quad (5)$$

where q_{net} is the net heat flux, σ is the Stephan Boltzmann constant, T_1 and T_2 are the surface temperatures in K, ε_1 and ε_2 are the emissivities of surfaces 1 and 2 (post irradiation viewing of fuel compacts, graphite surfaces, and stainless steel suggest that the emissivity not change with fluence), A_1 and A_2 are the areas of surfaces 1 and 2, and F_{12} is the view factor from surface 1 to 2. Radiation view factors for parallel disk to disk, ring to ring, and inside to outside of annulus were calculated using standard radiation view factor textbooks and implemented across each radial and axial gap. The emissivity of the graphite, grafoil, and graphite felt was assumed to be 0.9, 0.4 for stainless steel, and zirconia and zirconium at 0.5.

The neon gas fraction for each day was calculated for each capsule using average daily flow rates for helium and neon through each capsule.

Graphite and fuel compact material properties vary with neutron fluence. Fluence was imported from the detailed physics daily as-run calculations. The Abaqus Field Variable model was implemented where the neon fraction was taken as Field

Variable 1, and fast neutron fluence was taken as Field Variable 2. Thus, Abaqus provides a method of the thermal conductivity and gap conductance properties being able to vary with fields (neon fraction and fluence) and not only temperature.

The gamma/neutron heating for the various components (including the fuel compacts) were taken from the as-run physics calculations. Typical heat rates for the fuel compacts and graphite components were nominally 120×10^6 and 10×10^6 W/m^3 respectively. The test train heat rates exhibit the typical chopped cosine profile that is distinctive of ATR.

All gas gaps were modeled as changing with fast neutron fluence. This was accomplished by having the gas gap conductivity of each capsule change with fast neutron fluence accounting for the radius of each annulus changing during irradiation. The original finite element mesh models created in Abaqus were done with the as-built dimensions for the gas gaps. The gas gaps were assumed to be the hot gas gap dimension for gaps Gaps 1, 2, and 3, (see gap numbering in Fig. 3) as the hot gas gap dimension and room temperature gas gap dimension being virtually the same. Gap 4 takes into account the thermal expansion of the graphite sink and the stainless steel capsule. Experimental measurements [15] performed in a hot cell of the irradiated graphite annuli obtained from the post irradiation examination (PIE) measurements of the AGR-3/4 experiment were used. Uncertainties of 12.7×10^{-6} m are noted in Stempien et al.'s 2016 report [15]. Dimensional changes for the individual compacts, matrix, and PCEA and IG-110 graphite are shown in Fig. 10, Fig. 11, Fig. 12 and Fig. 13. Table 3 shows the $\Delta r/r$ divided by the fast neutron fluence at the end of irradiation for

the compacts and the rings. Capsules 1, 3, and 11 used a positive change in the inner radius of the sink. The sink was broken in disassembly for Capsule 11.

Fig. 10 shows the compact diameter change versus fast neutron fluence for Capsules 1, 3, 7, 8, 10, and 12. The remaining capsules used a linear curve fit of these capsules mentioned above and have not yet been measured as they are undergoing additional thermal testing. This is noted in Table 3 in the compact column where Capsules 2, 4, 5, 6, 9 and 11 all have the same slope. Fig. 11 depicts the diametric change in the matrix. The inside diameter is increasing with fluence, while the outside diameter is decreasing with fluence. The neutron damage is causing the annulus to shrink towards its center. Fig. 12 shows the change for the graphite ring. The matrix ring and the graphite ring both display similar behavior with the inside diameter expanding and the outer diameter contracting. Fig. 13 displays the change in diameter for the sink varying with fluence. Two of the inside diameters for the sink layer expand outwards, while all the rest contract inwards. These two points appear to be outliers as there is no good explanation for them being positive. All of the outer diameters contract inwards. In summary, all three annuli have contracting outer diameters, while the inner two have expanding inner diameters and the outer (sink) layer has the inner diameters contracting. While it is not the purpose of this article to investigate this phenomenon, it appears that a ratio exists of annulus thickness divided by radius where this transition occurs that the inner diameters contract inwards.

A line was drawn from zero to each individual point on these curves. The path that the diameters change during irradiation follows each individual line for each inner

and outer diameter. This was the only reasonable assumption that could be made as to how the diameters went from the start to the finish. An attempt was made to make a generalized curve fit, but it resulted in some of the gas gaps entirely closing for portions of the irradiation.

The coefficient of thermal expansion of the graphite varies with temperature and fluence as noted in Burchell and Eatherly's 1991 article [16]. The gap conductance for the inner three gaps is calculated by Equation (6):

$$gap1,2,3 = r_0\left(1+\frac{\Delta r}{r}\right)_{outer} - r_0\left(1+\frac{\Delta r}{r}\right)_{inner} \quad (6)$$

where r_0 is the unirradiated radius and $\Delta r/r$ varies for each separate inner and outer diameter. Values in Table 3 are per unit of fluence, so each value needs to be multiplied by the corresponding fluence to obtain the $\Delta r/r$. For example, Capsule 4 gap2 starts out at 63.5 × 10^{-6} m as shown in Table 3, and at a fast fluence of 6.0 × 10^{25} n/m^2 (multiply by 6.0), the gap has grown to 523× 10^{-6} m. The gap distance of Gap 4 between the sink and stainless steel capsule uses Equation (7) taking into account the thermal expansion of the graphite and stainless steel, and the graphite shrinkage due to irradiation.

$$gap4 = \{r_0[\alpha(T_i - T_0)+1]\}_{ss} - \left\{r_0\left[1+\frac{\Delta r}{r}+\alpha(T_i - T_0)\right]\right\}_{sink} \quad (7)$$

where α is the coefficient of thermal expansion varying with temperature and fast neutron fluence for the graphite as shown in Fig. 14, and $\Delta r/r$ is a function of

fluence as shown in Fig. 13. For graphite, α = 4.0 × 10^{-6} 1/K, and for stainless steel α = 17.3 × 10^{-6} 1/K. This coefficient for graphite would traditionally be 5.0 × 10^{-6} 1/K, but was adjusted to 4.0 × 10^{-6} 1/K to help align the TC temperatures with predicted temperatures. By using this lower value of thermal expansion of the graphite, it made a larger gap and raised all of the temperature of all the rings and compact by a few degrees. Several different references have values ranging from 4.0 to 5.5 × 10^{-6} 1/K. The other choice would have been to adjust the outer diameters of the sink based on the fluence. This was not done since good measurements were taken before and after irradiation at room temperature.

RESULTS

Fig. 15 through Fig. 20 show a small sampling of the results for the entire irradiation of seven ATR cycles: 151A, 151B, 152B, 154A, 154B, 155A, and 155B. Fig. 15 and Fig. 16 show temperature contours of the various components, while Fig. 17 through Fig. 20 show historical temperature results.

A cutaway view of the temperature contours and mesh are shown for Capsule 12 (typical) in Fig. 15. Fuel compact temperature maximum is 887°C at the center. Outside stainless steel capsule temperatures are near the temperature of the ATR primary coolant water temperature of 50°C. Gamma heating in the stainless steel end cap shows a radial temperature gradient. Several insulating materials have been placed in the model to prevent heat from transferring in the axial direction and out the stainless steel

end caps. The majority of the heat for these capsules is deposited in the fuel compacts (~1/3) and the three graphitic ring layers (~2/3).

Fig. 16 shows temperature contour plots for (a) fuel compacts, (b) matrix, (c) graphite ring, and (d) graphite sink. One goal of this experiment is to have as uniform temperature as possible in the fuel compacts and graphite rings. The majority of the compact is between 820 to 870°C (green to dark orange) as shown in Fig. 16a. The very center is hottest with outside edges coolest as is typical for a heat generating cylinder with heat transfer on all sides.

The matrix ring temperature contours are shown in Fig. 16b. Almost the entire matrix ring is between 765 and 800°C. Similar results are shown in Fig. 16c for the graphite ring, with the vast majority at 748°C plus or minus 8°C. The highest temperature in this component is on the very bottom inside (not shown). This occurs since the fuel compacts, matrix ring, and graphite ring all sit on a thin layer of grafoil that is fairly conductive, yet non-reactive with the materials contacting it. Coolest temperatures are at the top outside corner.

Fig. 16d shows the graphite sink temperature contours without the top and bottom lid. Median temperature is 495°C with minimum and maximum minus and plus 15°C. Hot spots occur on the inside in the four locations where the through tubes prevent the heat from evenly transferring to the outside. Coolest temperatures are on the top outside edges next to the through tube holes. Gamma heating for all of these annular components was implemented in 90-degree segments. It appears that the azimuthal temperature variations are very small.

Fig. 17 shows a history plot of Capsule 4. There is not enough room to show all 12 capsules, but this one is fairly representative. The TCs are located in the center of the sink ring as shown in Fig. 3. The top panel shows the temperature history of the TCs, while the second panel shows the temperature difference of the measured TC minus calculated. These ΔT values are about 10°C for the first four cycles, then a gradual increase to about 60°C by the end of the final cycle. These are very good temperature predictions during the first four cycles. The model does not match the TCs during the last three cycles either because of TC drift or some aspect not being captured within the model. The third through fifth panel show the volume average (solid line) and minimum and maximum bands for the compacts, matrix, and ring, respectively. The goal of the experiment was to maintain each layer as close to level as possible. As irradiation progresses, the fuel in the compacts burned out, the graphite rings shrunk, it was difficult to maintain level temperatures. A gradual increase in the TC set point during the last two cycles helped boost the ring and matrix temperatures. This was accomplished by adjusting the gas mixture until the TCs matched the desired TC set points. Thermal model predictions were performed during the experiment to help determine the TC set points.

Time average volume average (TAVA) history plots are presented in Fig. 18 for Capsule 4. TAVA was calculated by first calculating the volume average temperature for each compact for each time step. The volume average temperature for each time step (day) was then summed up for each day and divided by the total number of days. This capsule was selected to show results as it is very average. Each panel shows the time

average minimum, time average maximum, and time average volume average. The top panel shows the compacts, second panel matrix, third panel graphite ring, and fourth panel for the graphite sink ring. The compacts are very level throughout. The reason no burnup effect shown is that the northeast lobe power in ATR was adjusted up during irradiation. The matrix ring sinks a little toward the end of irradiation, while the ring drops off almost 40°C from its peak near 100 effective full-power days (EFPD). The sink is very level throughout. Experience has shown that these TAVA values at the end of irradiation are the temperature value of interest for fuel and graphite performance.

Fig. 19 shows a description of the cut-away view for the contour plot in Fig. 20. The views are looking straight into an east/west cut (looking straight north) on the right side of the compact, matrix, and ring. A time step during each cycle was selected that showed the single day in which the compact volume-average temperature was closest to the cycle TAVA temperature. Fig. 20 shows how the cycle average temperature varies with position (elevation and radius) during irradiation.

Fig. 20 shows a contour plot for the compacts on the top, matrix in the middle, and ring on the bottom for each ATR cycle for Capsule 4. A constant temperature legend is displayed for each compact, matrix, and ring. As mentioned above, these contour plots were taken from a single day that had the closest compact volume average fuel temperature to the entire cycle average. These plots may be used in PIE to determine two and three dimensional constant temperature profiles. This may help when examining for certain fission products that might condense out on these constant

temperature areas within a graphite layer. A detailed diffusion analysis with these calculated temperatures would be necessary to track fission product migration.

CONCLUSIONS

A daily as-run thermal analysis has been performed for the AGR-3/4 fuel experiment for all 12 capsules during the entire ATR irradiation of the experiment. A variable gas gap model changing with fast neutron fluence from PIE measurements was implemented. A three-dimensional finite element heat transfer model was created to simulate this experiment in the ATR. Volumetric heat rates and fast neutron fluence were imported from a daily as-run detailed physics analysis. Thermal conductivity of the fuel compacts and graphite holders varied with fluence and temperature. Daily helium-neon gas mixtures were implemented into the 12 models. Temperature contours of various components have been presented. Daily history plots of actual TC measurements have been compared to simulated results with these models for Capsule 4 for the entire irradiation. The temperature predictions appear to correlate fairly closely with the actual TC measurements. The goal of these predictions is to be able to predict temperature profiles in each graphite layer on a daily basis and on a time average volume average basis. Temperature contour plots have been presented showing a cross sectional view of the compacts, matrix, and ring for all seven ATR cycles. These contours may be used in PIE for tracking fission products in the various layers.

COPYRIGHT STATEMENT

ACKNOWLEDGMENT

Work supported by the U.S. Department of Energy, NGNP Program, Idaho Operations Office Contract DE-AC07-05ID14517.

FUNDING

Funding supported by the U.S. Department of Energy, Advanced Reactor Technologies Program, Idaho Operations Office Contract DE-AC07-05ID14517.

NOMENCLATURE

A	radiation surface area, m^2
dpa	displacements per atom
E_n	neutron energy, MeV
F_{12}	view factor from surface 1 to 2
k	thermal conductivity, W/m·K
MeV	million electron volts, MeV
MW	molecular weight
q	heat flux, W/m^2
$\dot{q}$	volumetric heat rate, W/m^3
T	temperature, K
x,y,z	Coordinates, m

Greek Letters

α	coefficient of thermal expansion, 1/K
Δr	change in radius, m
ϕ	particle packing fraction
Γ	fast neutron fluence, n/m^2
σ	Stefan-Boltzmann constant, $W/m^2 \cdot K^4$
ε	emissivity

Subscripts or Superscripts

DNE	dido nickel equivalent
e	effective
gas	gas mixture
i	instantaneous
inner	inner
irr	irradiated
m	matrix
n	neutron
net	net heat flux
outer	outer
o	original unirradiated
p	particle
sink	graphite sink ring
ss	stainless steel

Acronyms and Abbreviations

AGR	Advanced Gas Reactor
ATR	Advanced Test Reactor
DNE	Dido Nickel Equivalent

EFPD	Effective Full Power Day
EOI	End of Irradiation
MCNP	Monte Carlo N-Particle
FF	Fast Fluence
INL	Idaho National Laboratory
ID	Inside Diameter
OD	Outside Diameter
PIE	Post Irradiation Examination
TAVA	Time Average Volume Average
TC	Thermocouple
TRISO	Tristructural-Isotropic

REFERENCES

[1] Hawkes, G. L., Sterbentz, J. W., Maki, J. T., Pham, B. T., "Daily Thermal Predictions of the AGR-1 Experiment with Gas Gaps Varying with Time," paper # 12111, ICAPP 2012 Conference, Chicago, IL, June 2012.

[2] Hawkes, G. L., Sterbentz, J. W., Pham, B. T.,, "Thermal Predictions of the AGR-2 Experiment with Variable Gas Gaps," Nuclear Technology, MS# NT14-73R1, accepted October 2014.

[3] Hawkes, G. L., Sterbentz, J. W. , Maki, J. T., "Thermal Predictions of the AGR-3/4 Experiment," paper # IMECE2013-65155, ASME 2013 International Mechanical Engineering Congress & Exposition, San Diego, CA, Nov 16-21, 2013.

[4] Hawkes, G. L., Sterbentz, J. W., Maki, J. T., "Thermal Predictions of the AGR-3/4 Experiment with Time Varying Gas Gaps," ASME J of Nuclear Rad Sci 1(4), 041012, 2015 Paper No: NERS-15-1006; doi: 10.1115/1.4030046.

[5] Dassault Systèmes, ABAQUS version 6.14-2, www.simulia.com or www.abaqus.com, Providence, Rhode Island, 2014.

[6] Sterbentz, J. W., Hawkes, G. L., Maki, J. T., Petti, D. A., "Monte Carlo Depletion Calculation for the AGR-1 TRISO Particle Irradiation Test," paper 1308, ANS Annual Conference, San Diego, CA, June 2010.

[7] Hawkes, G. L., Sterbentz, J. W., Pham, B. T., "Sensitivity Evaluation of the AGR-3/4 Experiment Thermal Model Irradiated in the Advanced Test Reactor," paper # IMECE2015-53544, ASME 2015 International Mechanical Engineering Congress & Exposition, Houston, TX, Nov 13-19, 2015.

[8] Gontard, R., Nabielek, H., "Performance Evaluation of Modern HTR TRISO Fuels," Forschungszentrum Jülich GmbH, HTA-IB-05/90, July 31, 1990.

[9] Konings, R. J. M., Editor in Chief, "Comprehensive Nuclear Materials, Volume 4, Radiation Effects in Structural and Functional Materials for Fission and Fusion Reactors," Section 4.11.5.7 Table 9, ISBN: 978-0-08-056033-5, 2012 Copyright Elsevier.

[10] Gonzo, E. E., 2002, "Estimating Correlations for the Effective Thermal Conductivity of Granular Materials," Chem. Eng. J., 90(3), pp. 299–302.

[11] Windes, W. E., "Data Report on Post-Irradiation Dimensional Change in AGC-1 Samples," INL/EXT-12-26255, June 2012.

[12] Snead, L. L., Burchell, T. D., "Reduction in Thermal Conductivity Due to Neutron Irradiation, 22nd Biennial Conference on Carbon, Extended Abstracts (1995) 774-775.

[13] Sterbentz, J. W., "Fast Flux to DPA Multiplier," E-mail communication to G.L. Hawkes, August 5, 2009.

[14] Kestin, J., Knierim, K., Mason, E. A., Najafi, B., Ro, S. T., Waldman, M., "Equilibrium and Transport Properties of the Noble Gases and Their Mixtures at Low Density," J. Phys. Chem, Vol. 13, No. 1, pp 229-303, 1984.

[15] Stempien, J. D., Rice, F. J., Winston, P. L., Harp, J. M., "AGR-3/4 Irradiation Test Train Disassembly and Component Metrology First Look Report," INL/EXT-16-38005 Rev 0, March 2016

[16] Burchell, T. D., Eatherly, W. P., "The Effect of Radiation Damage on the Properties of GraphNOL N3M," Journal of Nuclear Materials, 179-181 (1991) 205-208.

Figure Captions List

Fig. 1 ATR core cross section showing the northeast flux trap position containing the AGR-3/4 experiment

Fig. 2 Axial view of two AGR-3/4 capsules

Fig. 3 Cross-sectioned view of an AGR-3/4 capsule

Fig. 4 Three dimensional cutaway rendering of single AGR-3/4 capsule

Fig. 5 Cutaway view of finite element mesh of AGR-3/4 capsule with colored entities

Fig. 6 Three-dimensional plot of AGR-3/4 fuel compact thermal conductivity (W/m-K) varying with fluence and temperature

Fig. 7 Three-dimensional plot of AGR-3/4 matrix thermal conductivity (W/m-K) varying with fluence and temperature

Fig. 8 Graphite thermal conductivity plot of ratio of irradiated over unirradiated (kirr/ko) varying with temperature and dpa

Fig. 9 Helium-Neon gas thermal conductivity versus temperature and mole fraction helium

Fig. 10 Compact diameter change versus fluence from PIE measurements

Fig. 11 Matrix ring ID and OD change versus fluence from PIE measurements

Fig. 12 Graphite ring ID and OD change versus fluence from PIE measurements

Fig. 13 Sink ID and OD change versus fluence from PIE measurements

Table Caption List

Table 1 As-built dimensions for compact, matrix, graphite ring, sink, and capsule for all 12 capsules

Table 2 As-built dimensions for all four temperature control gas gaps for all 12 capsules

Table 3 Slope of dimensional change for compacts, inner and outer rings, and sink. (Dimensional change ($\Delta r/r$) at end of irradiation divided by fast neutron fluence at end of irradiation, units are ($\Delta r/r$)/fluence, or 1/fluence), or $(m^2/n) \times 10^{25}$

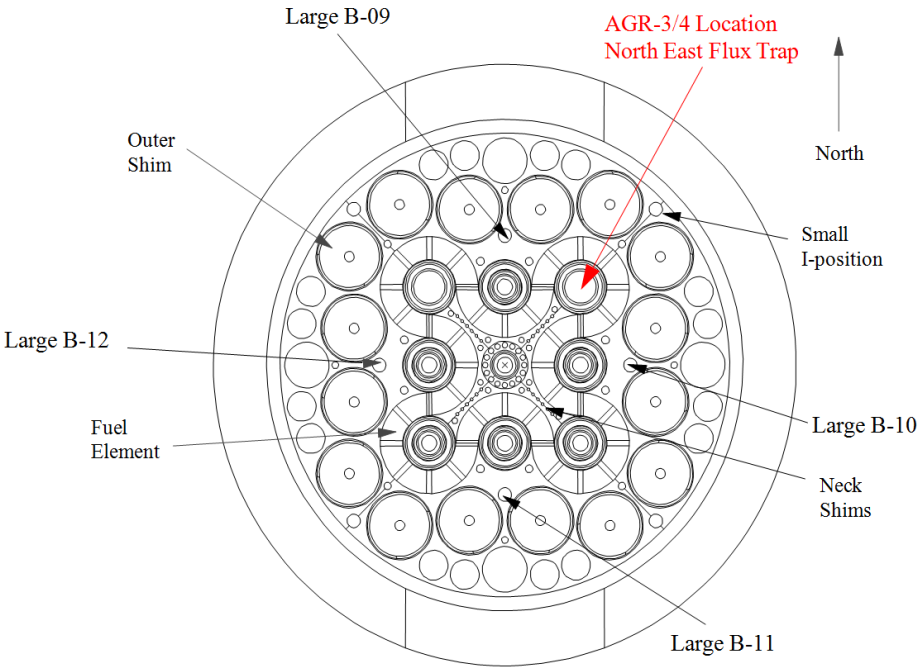
Large B-09
AGR-3/4 Location
North East Flux Trap
North
Outer
Shim
Small
I-position
Large B-12
Fuel
Element
Large B-10
Neck
Shims
Large B-11

Fig. 1

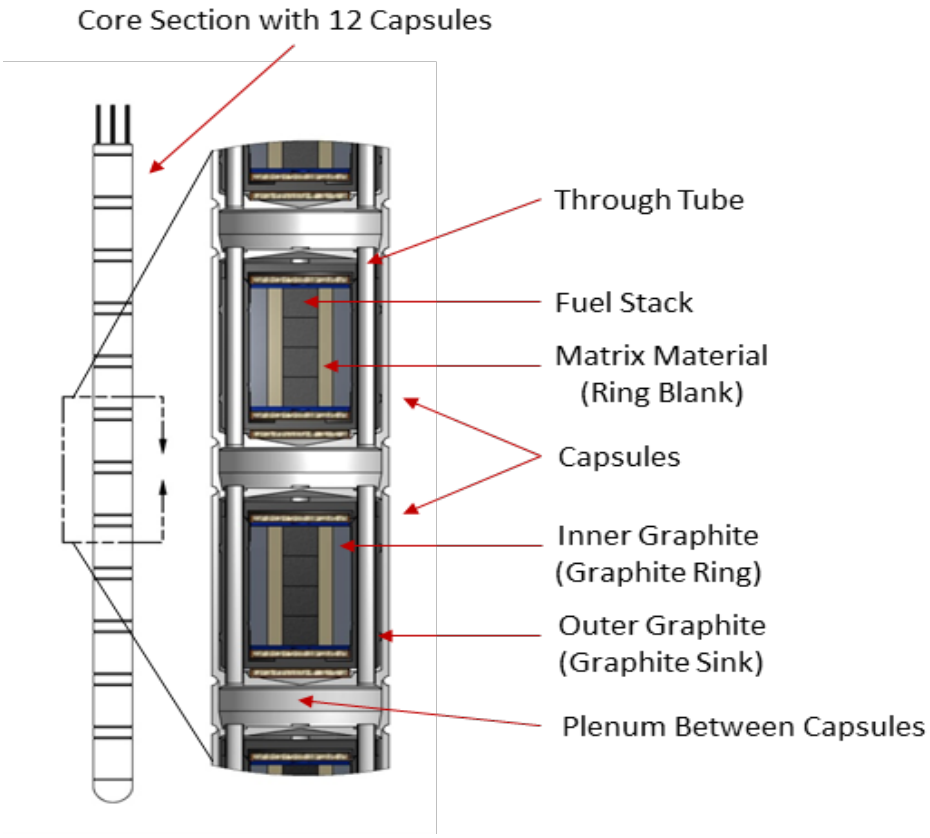
Core Section with 12 Capsules
Through Tube
Fuel Stack
Matrix Material
(Ring Blank)
Capsules
Inner Graphite
(Graphite Ring)
Outer Graphite
(Graphite Sink)
Plenum Between Capsules

Fig. 2

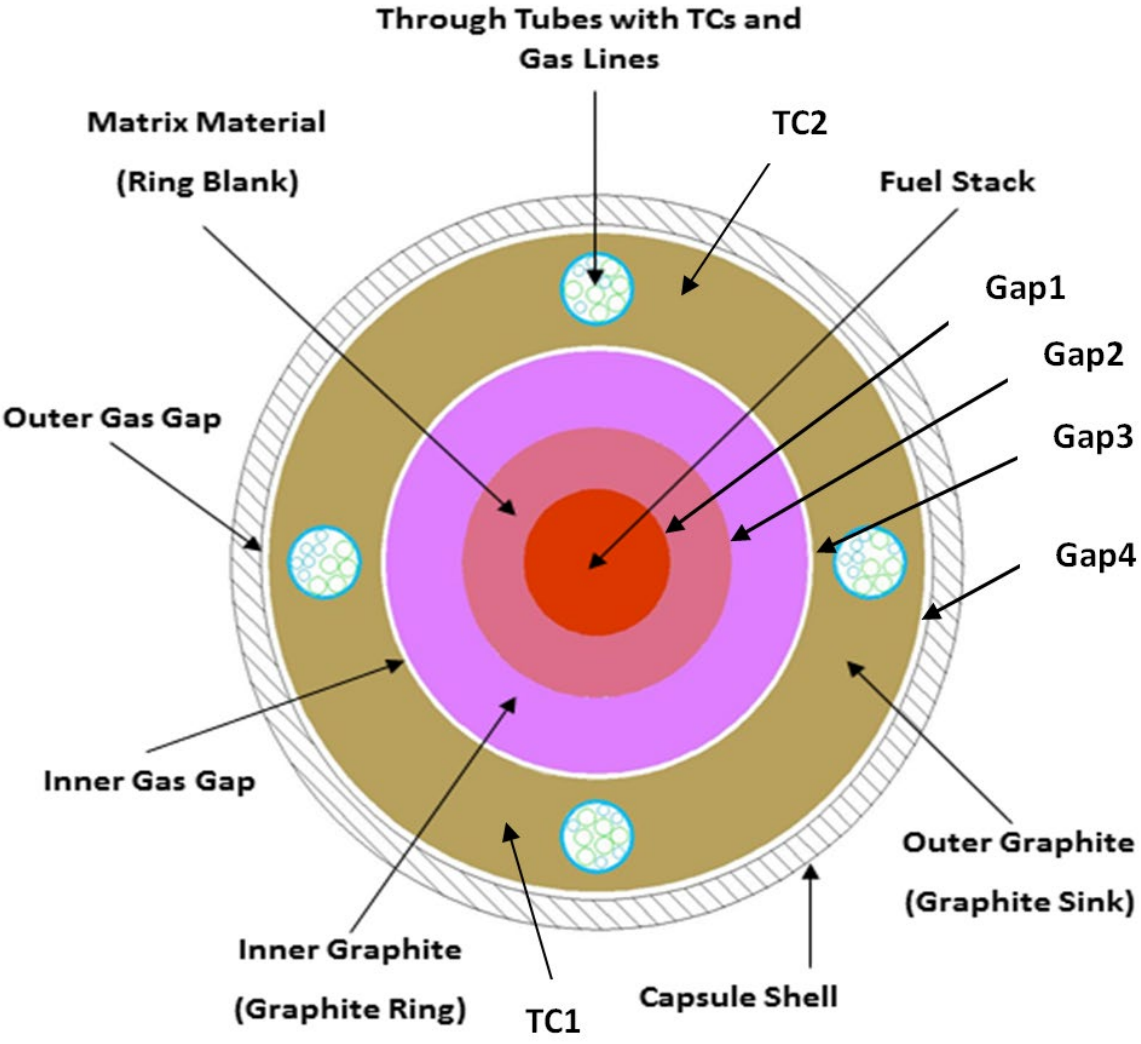
Through Tubes with TCs and Gas Lines
Matrix Material (Ring Blank)
TC2
Fuel Stack
Gap1
Gap2
Gap3
Gap4
Outer Gas Gap
Inner Gas Gap
Outer Graphite (Graphite Sink)
Inner Graphite (Graphite Ring)
TC1
Capsule Shell

Fig. 3

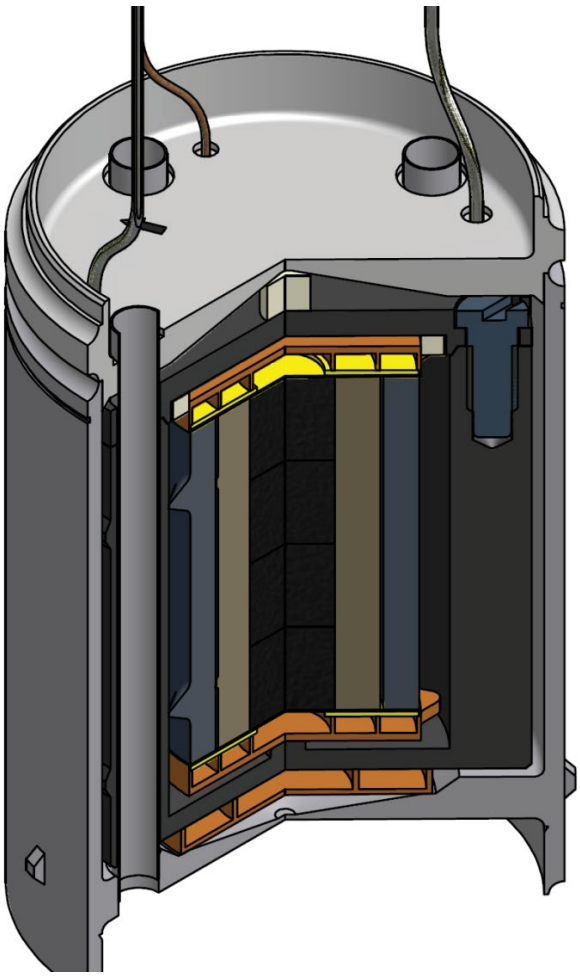

Fig. 4

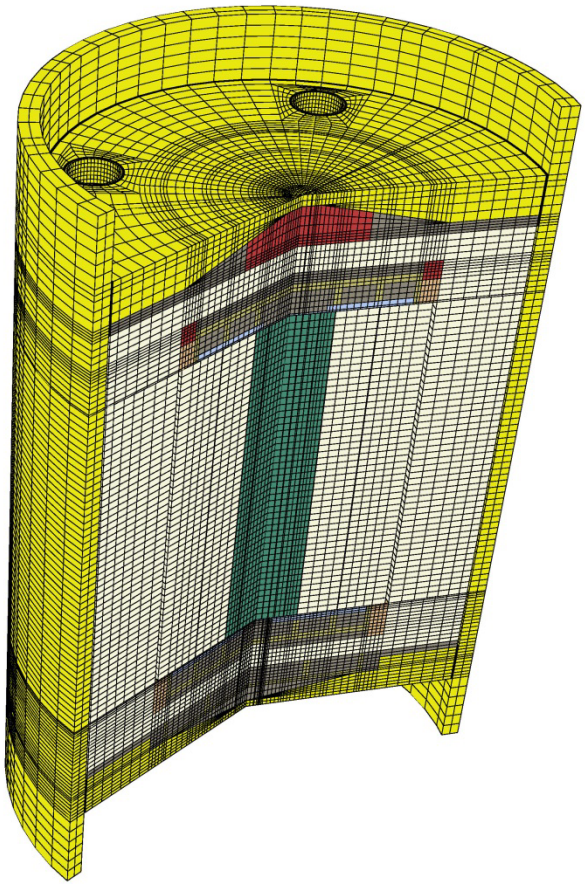

Fig. 5

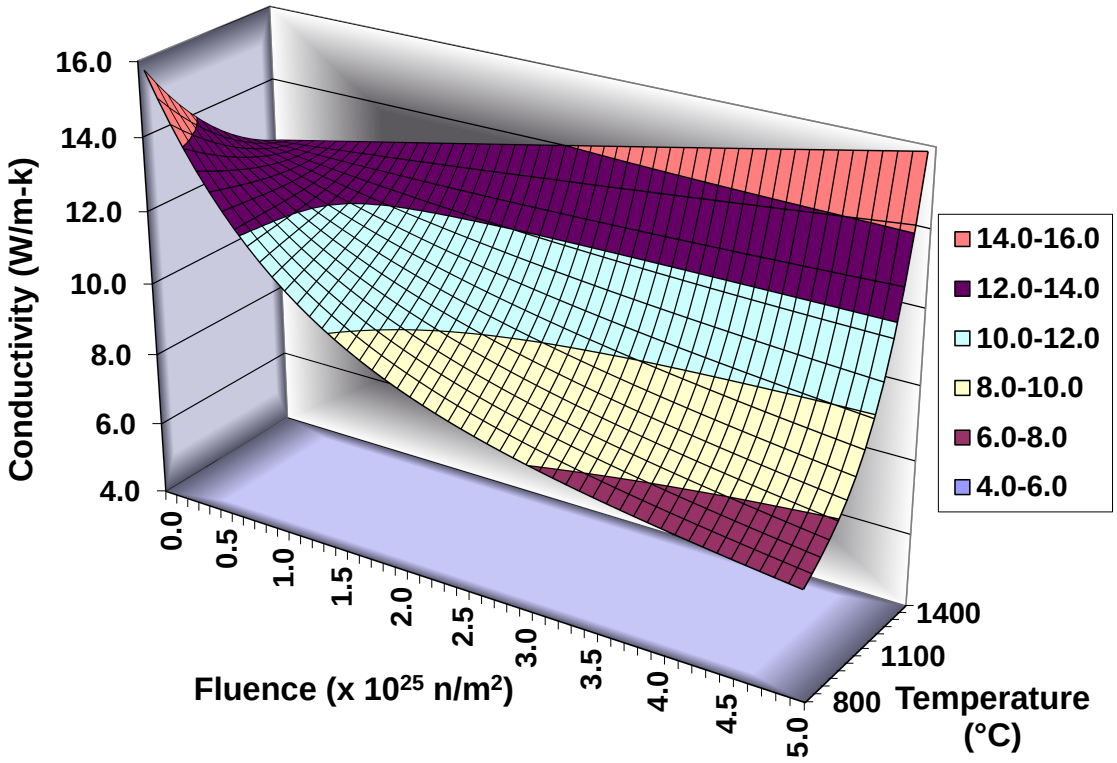
Conductivity (W/m-k)
16.0
14.0
12.0
10.0
8.0
6.0
4.0
0.0
0.5
1.0
1.5
2.0
2.5
3.0
3.5
4.0
4.5
5.0
Fluence (x 10^25 n/m^2)
1400
1100
800
Temperature (°C)
14.0-16.0
12.0-14.0
10.0-12.0
8.0-10.0
6.0-8.0
4.0-6.0

Fig. 6

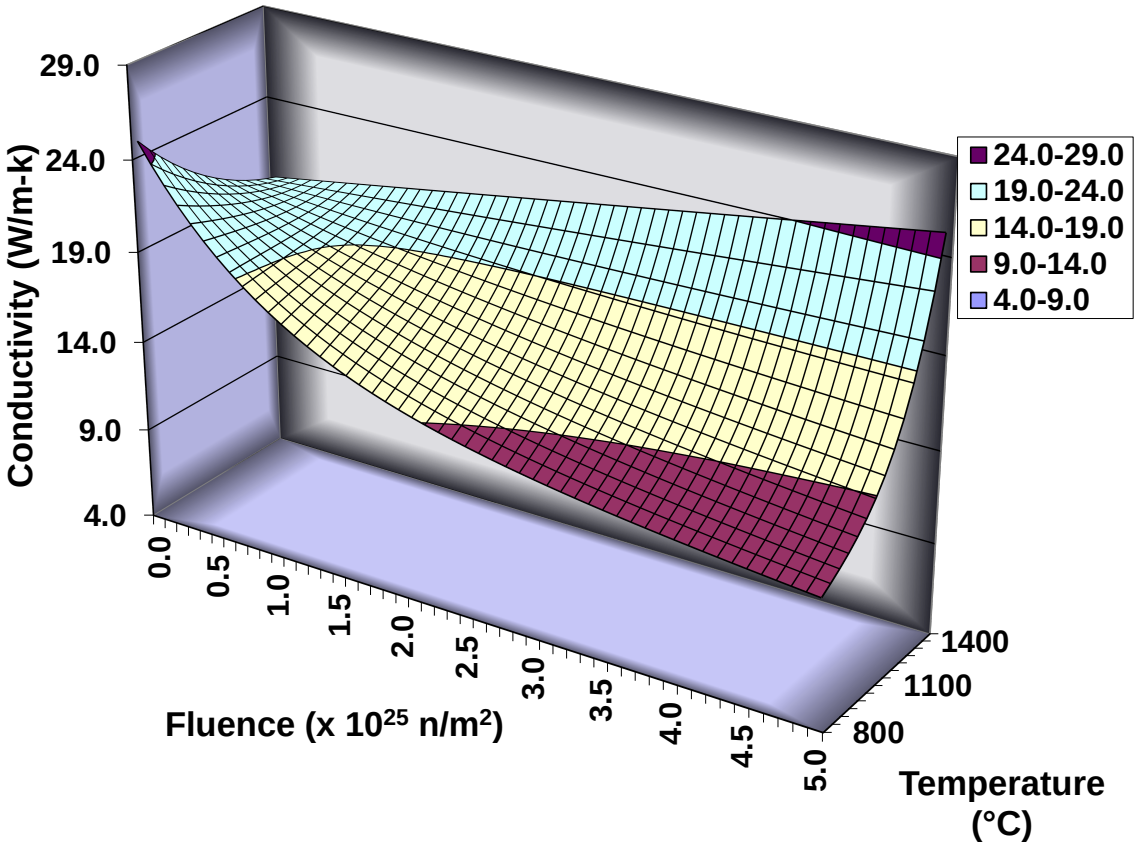
Conductivity (W/m-k)
29.0
24.0
19.0
14.0
9.0
4.0
24.0-29.0
19.0-24.0
14.0-19.0
9.0-14.0
4.0-9.0
0.0
0.5
1.0
1.5
2.0
2.5
3.0
3.5
4.0
4.5
5.0
Fluence (x 10^25 n/m^2)
1400
1100
800
Temperature (°C)

Fig. 7

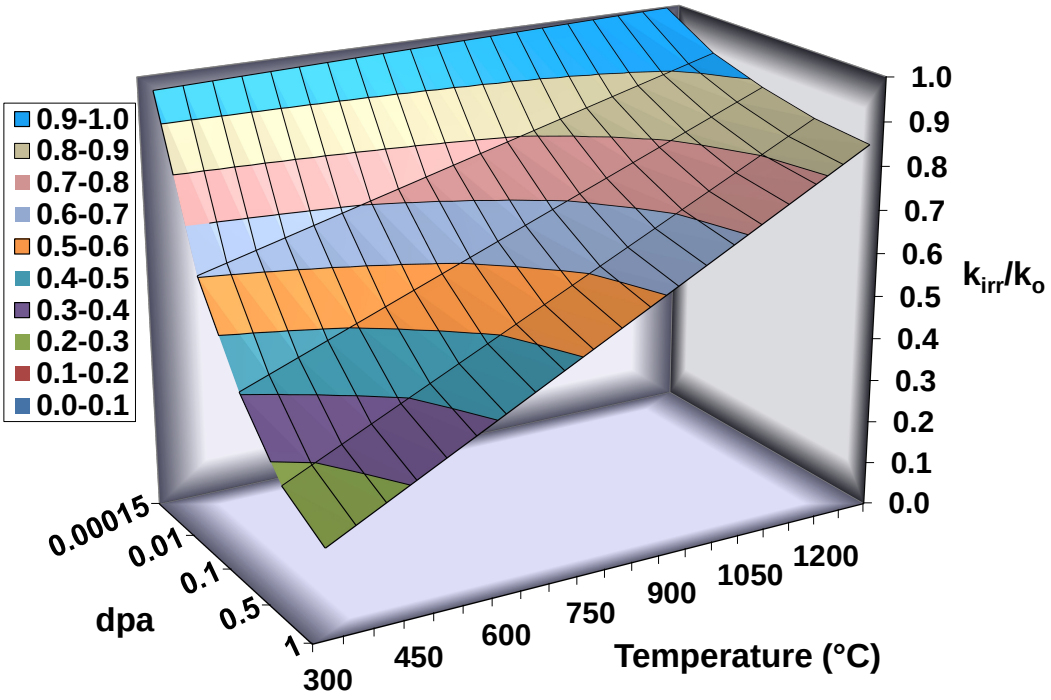
0.9-1.0
0.8-0.9
0.7-0.8
0.6-0.7
0.5-0.6
0.4-0.5
0.3-0.4
0.2-0.3
0.1-0.2
0.0-0.1
1.0
0.9
0.8
0.7
0.6
0.5
0.4
0.3
0.2
0.1
0.0
k_irr/k_o
0.00015
0.01
0.1
0.5
1
dpa
300
450
600
750
900
1050
1200
Temperature (°C)

Fig. 8

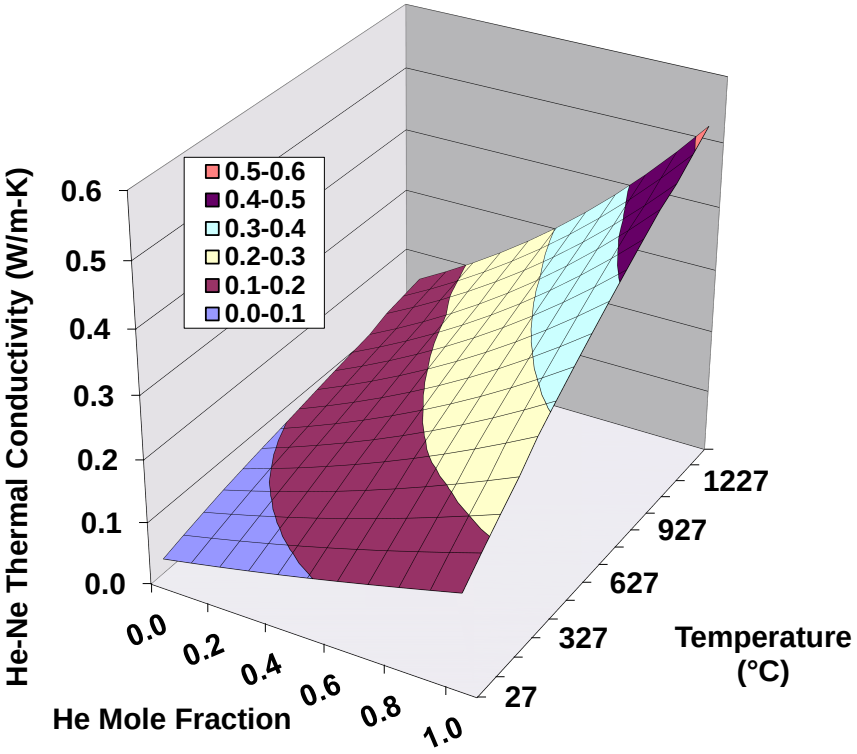
He-Ne Thermal Conductivity (W/m-K)
0.6
0.5
0.4
0.3
0.2
0.1
0.0
0.5-0.6
0.4-0.5
0.3-0.4
0.2-0.3
0.1-0.2
0.0-0.1
0.0
0.2
0.4
0.6
0.8
1.0
He Mole Fraction
1227
927
627
327
27
Temperature
(°C)

Fig. 9

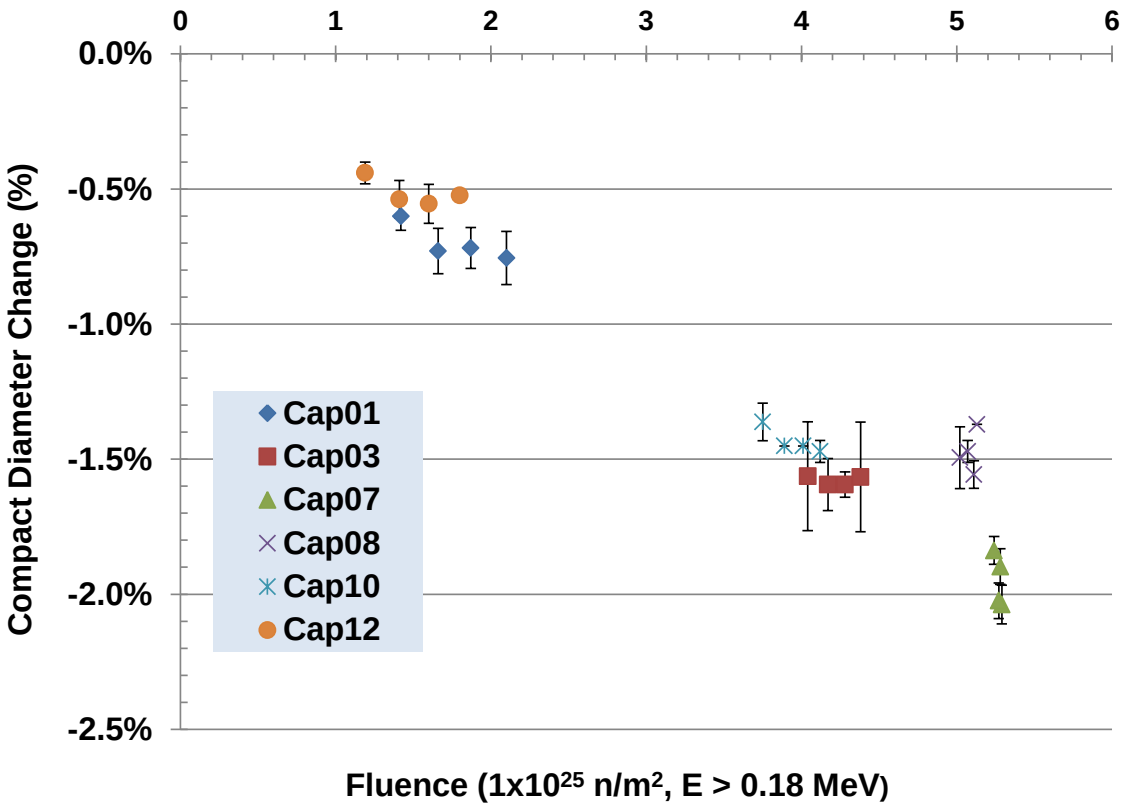
0
1
2
3
4
5
6
0.0%
-0.5%
-1.0%
-1.5%
-2.0%
-2.5%
Compact Diameter Change (%)
Cap01
Cap03
Cap07
Cap08
Cap10
Cap12
Fluence (1x10²⁵ n/m², E > 0.18 MeV)

Fig. 10

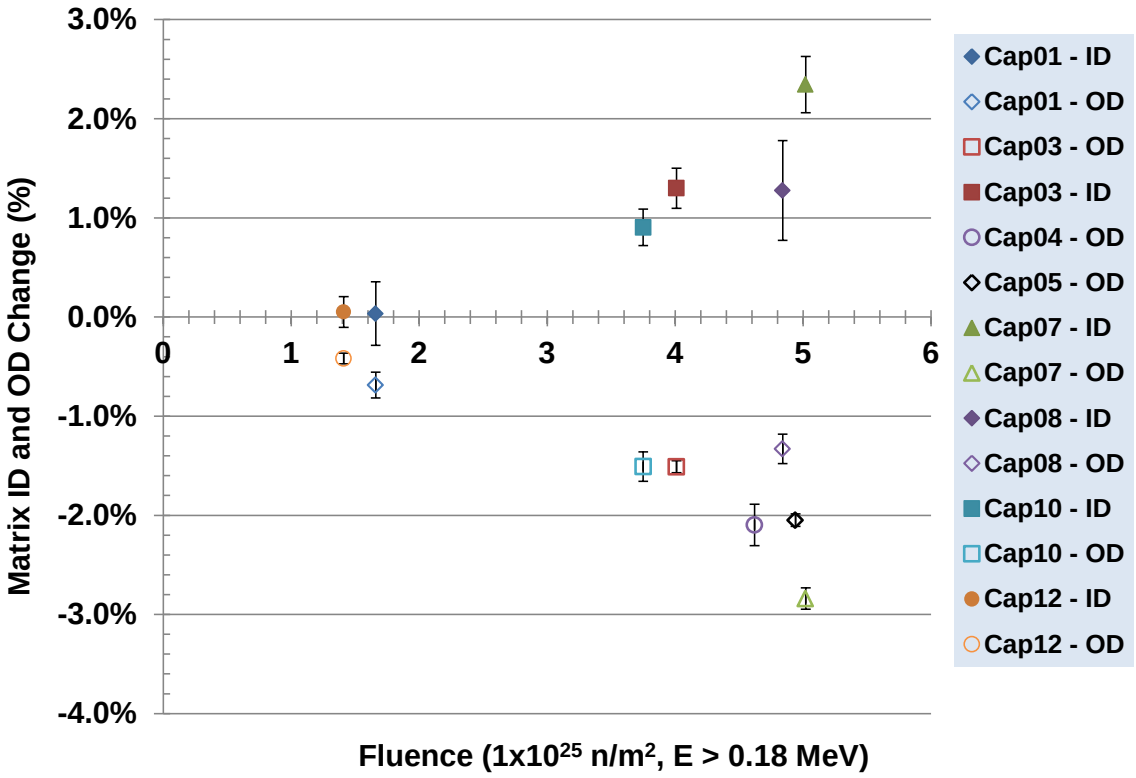
3.0%
2.0%
1.0%
0.0%
-1.0%
-2.0%
-3.0%
-4.0%
0
1
2
3
4
5
6
Matrix ID and OD Change (%)
Fluence (1x10^25 n/m^2, E > 0.18 MeV)
Cap01 - ID
Cap01 - OD
Cap03 - OD
Cap03 - ID
Cap04 - OD
Cap05 - OD
Cap07 - ID
Cap07 - OD
Cap08 - ID
Cap08 - OD
Cap10 - ID
Cap10 - OD
Cap12 - ID
Cap12 - OD

Fig. 11

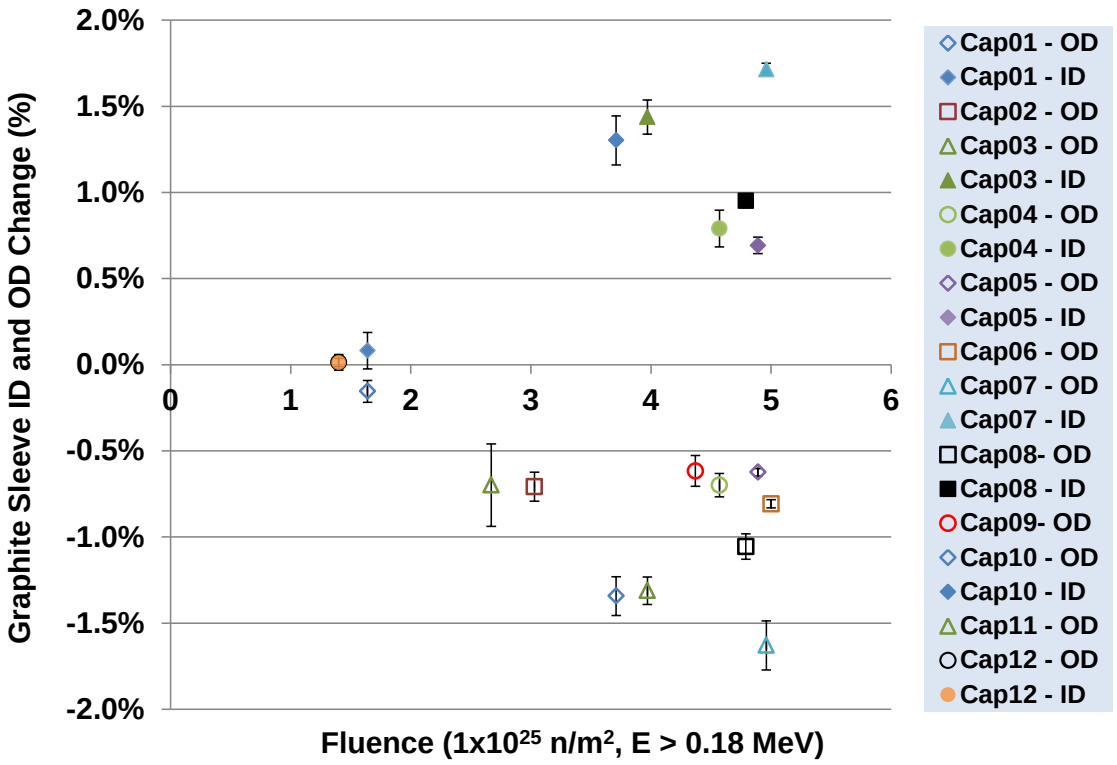
Graphite Sleeve ID and OD Change (%)
2.0%
1.5%
1.0%
0.5%
0.0%
-0.5%
-1.0%
-1.5%
-2.0%
0
1
2
3
4
5
6
Fluence (1x10^25 n/m^2, E > 0.18 MeV)
Cap01 - OD
Cap01 - ID
Cap02 - OD
Cap03 - OD
Cap03 - ID
Cap04 - OD
Cap04 - ID
Cap05 - OD
Cap05 - ID
Cap06 - OD
Cap07 - OD
Cap07 - ID
Cap08- OD
Cap08 - ID
Cap09- OD
Cap10 - OD
Cap10 - ID
Cap11 - OD
Cap12 - OD
Cap12 - ID

Fig. 12

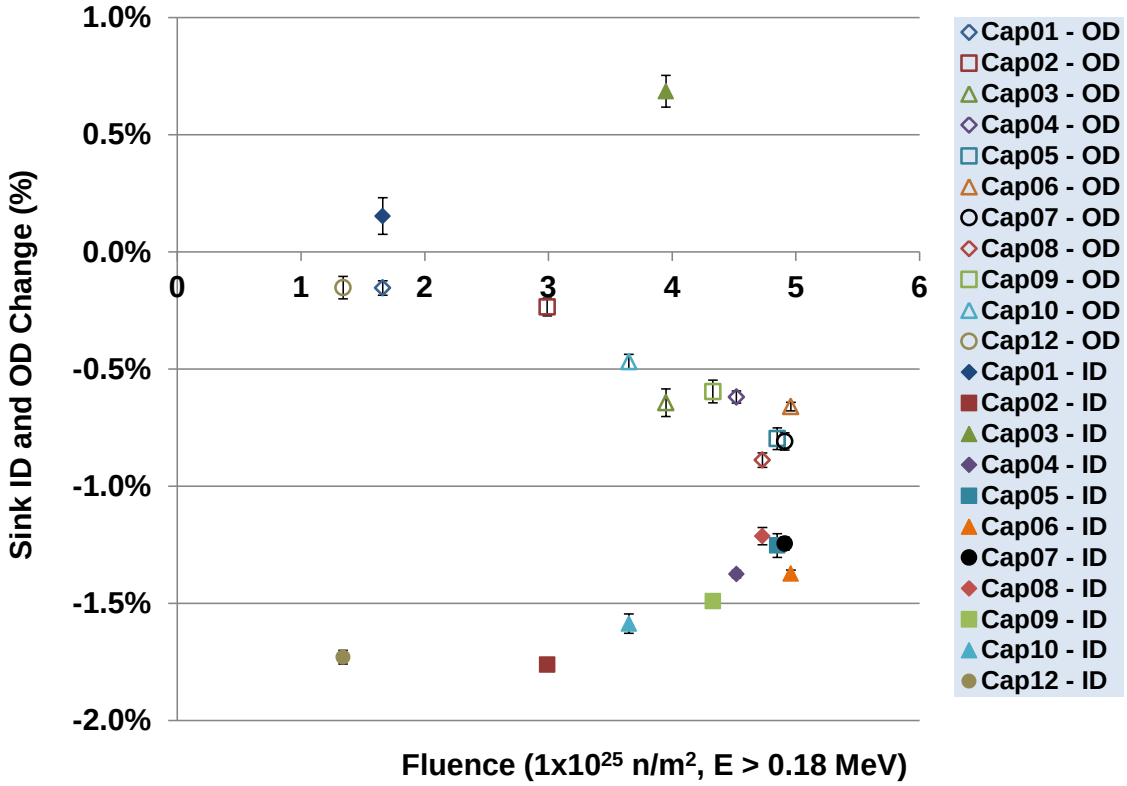
1.0%
0.5%
0.0%
-0.5%
-1.0%
-1.5%
-2.0%
0
1
2
3
4
5
6
Sink ID and OD Change (%)
Fluence (1x10²⁵ n/m², E > 0.18 MeV)
Cap01 - OD
Cap02 - OD
Cap03 - OD
Cap04 - OD
Cap05 - OD
Cap06 - OD
Cap07 - OD
Cap08 - OD
Cap09 - OD
Cap10 - OD
Cap12 - OD
Cap01 - ID
Cap02 - ID
Cap03 - ID
Cap04 - ID
Cap05 - ID
Cap06 - ID
Cap07 - ID
Cap08 - ID
Cap09 - ID
Cap10 - ID
Cap12 - ID

Fig. 13

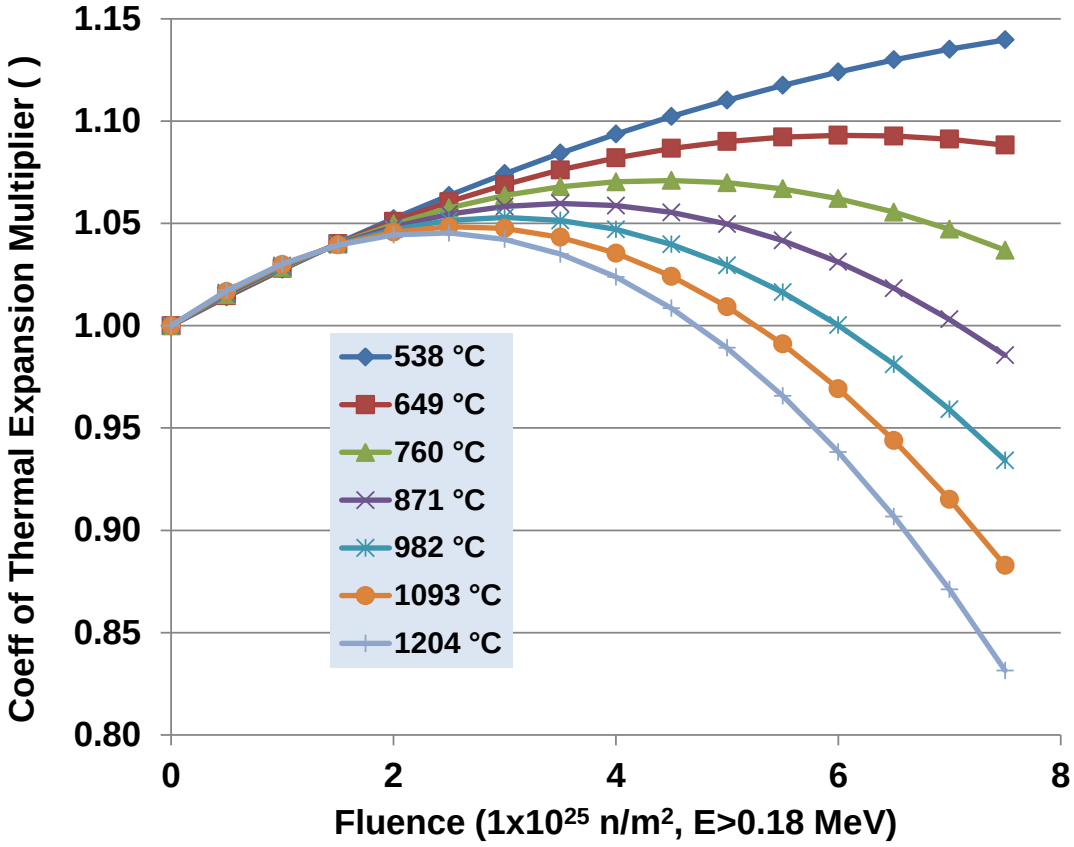
Coeff of Thermal Expansion Multiplier ( )
1.15
1.10
1.05
1.00
0.95
0.90
0.85
0.80
0
2
4
6
8
Fluence (1x10^25 n/m^2, E>0.18 MeV)
538 °C
649 °C
760 °C
871 °C
982 °C
1093 °C
1204 °C

Fig. 14

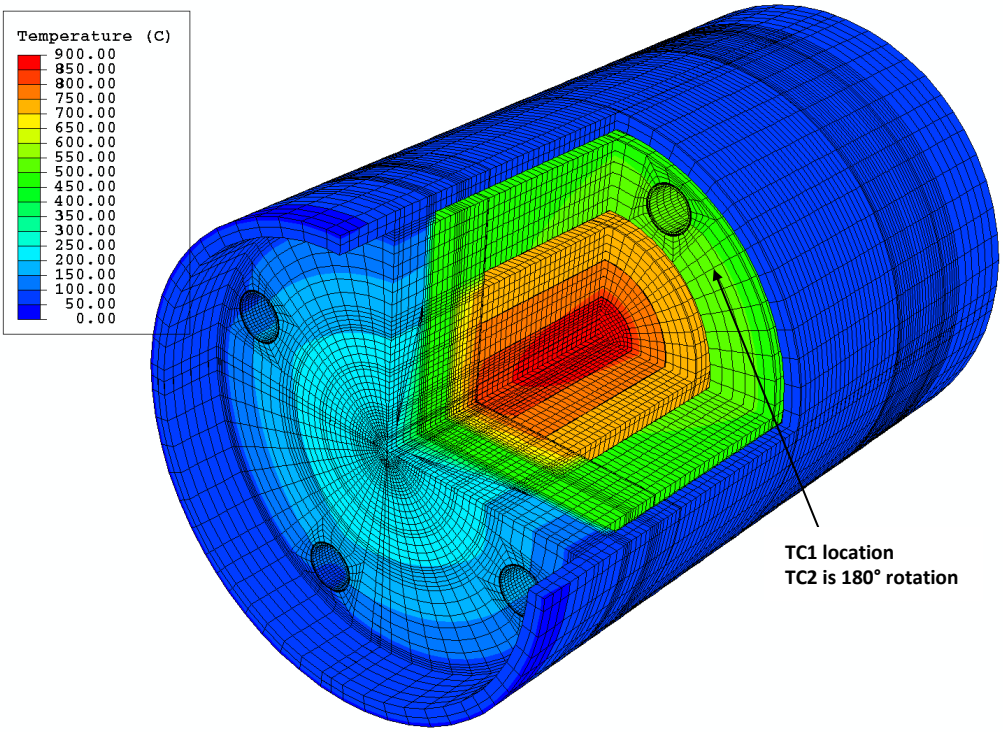
Temperature (C)
900.00
850.00
800.00
750.00
700.00
650.00
600.00
550.00
500.00
450.00
400.00
350.00
300.00
250.00
200.00
150.00
100.00
50.00
0.00
TC1 location
TC2 is 180° rotation

Fig. 15

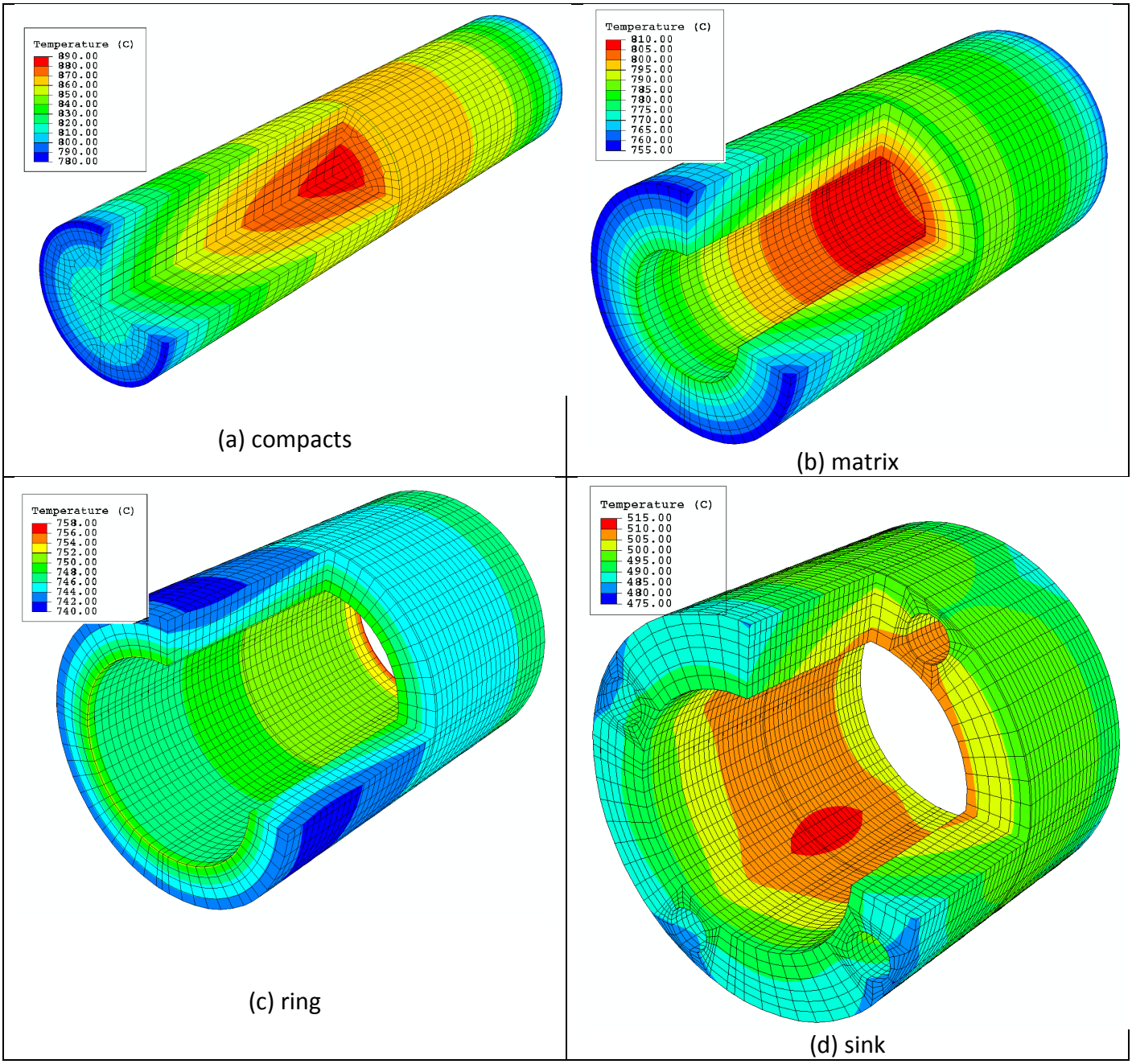
Temperature (C)
890.00
880.00
870.00
860.00
850.00
840.00
830.00
820.00
810.00
800.00
790.00
780.00
(a) compacts
Temperature (C)
810.00
805.00
800.00
795.00
790.00
785.00
780.00
775.00
770.00
765.00
760.00
755.00
(b) matrix
Temperature (C)
758.00
756.00
754.00
752.00
750.00
748.00
746.00
744.00
742.00
740.00
(c) ring
Temperature (C)
515.00
510.00
505.00
500.00
495.00
490.00
485.00
480.00
475.00
(d) sink

Fig. 16

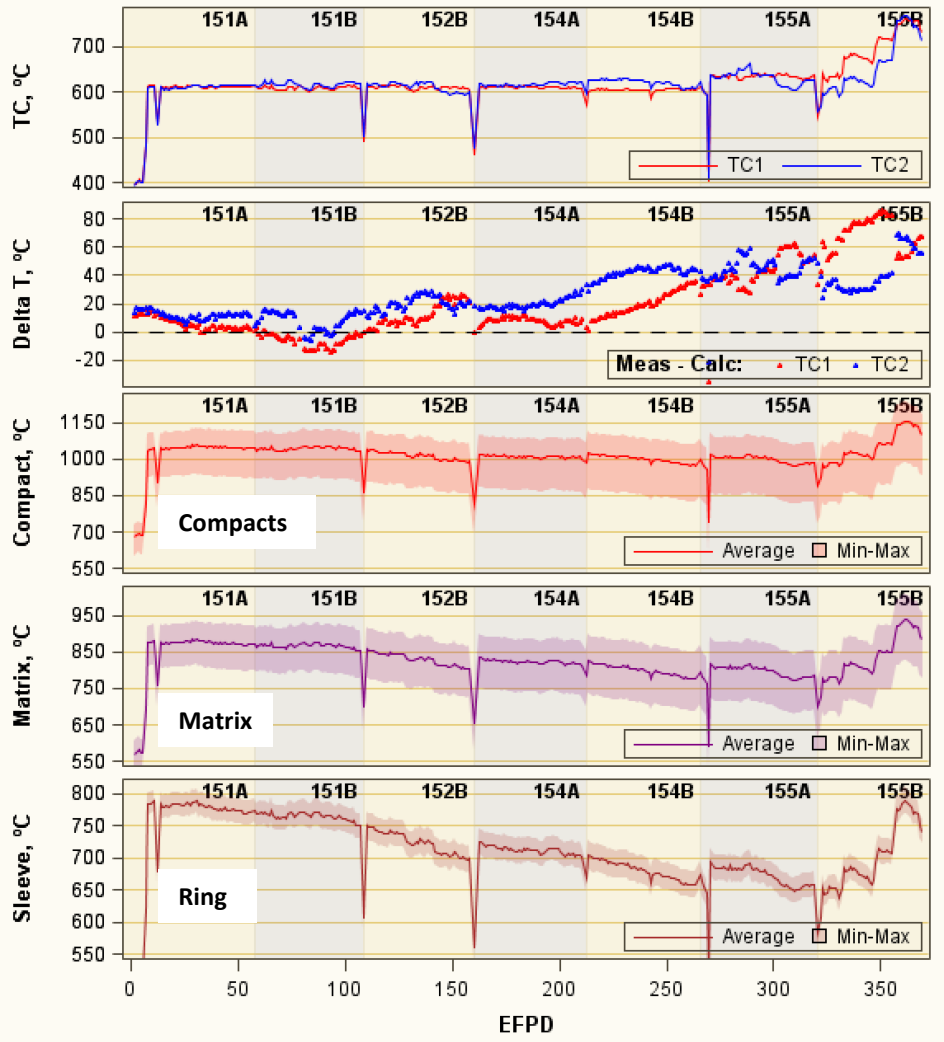
151A
151B
152B
154A
154B
155A
155B
TC, °C
700
600
500
400
TC1
TC2
Delta T, °C
80
60
40
20
0
-20
Meas - Calc:
TC1
TC2
Compact, °C
1150
1000
850
700
550
Compacts
Average
Min-Max
Matrix, °C
950
850
750
650
550
Matrix
Average
Min-Max
Sleeve, °C
800
750
700
650
600
550
Ring
Average
Min-Max
0
50
100
150
200
250
300
350
EFPD

Fig. 17

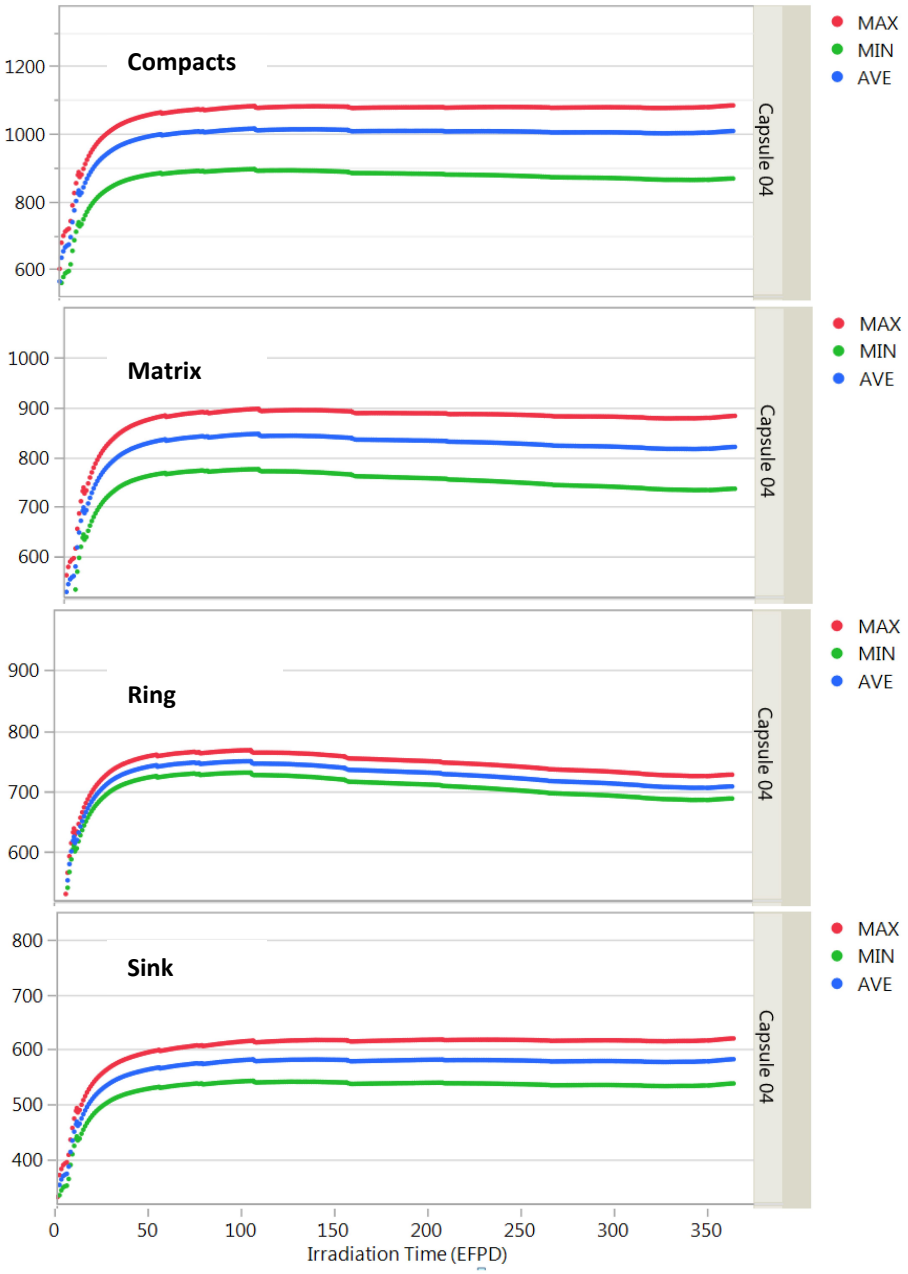
Compacts
Matrix
Ring
Sink
MAX
MIN
AVE
Capsule 04
1200
1000
800
600
900
700
500
400
0
50
100
150
200
250
300
350
Irradiation Time (EFPD)

Fig. 18

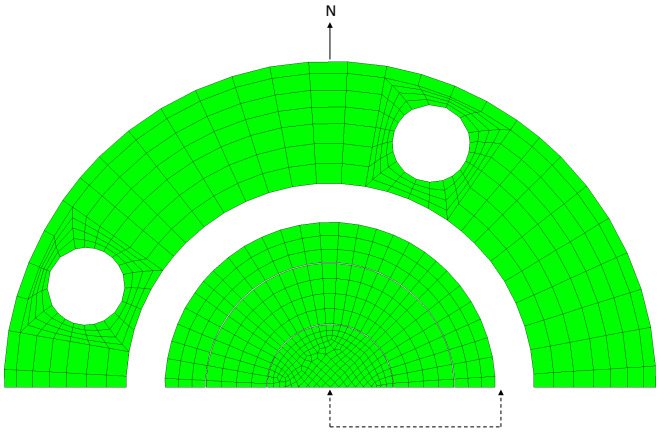

Fig. 19

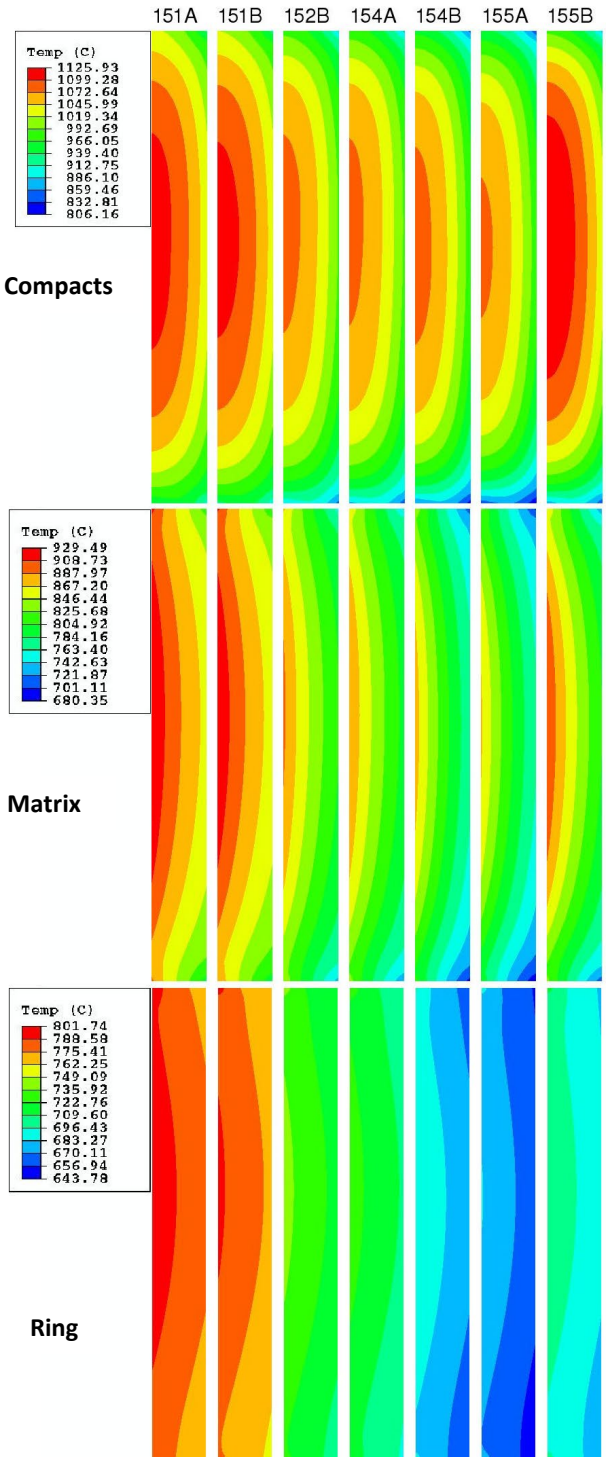
151A
151B
152B
154A
154B
155A
155B
Temp (C)
1125.93
1099.28
1072.64
1045.99
1019.34
992.69
966.05
939.40
912.75
886.10
859.46
832.81
806.16
Compacts
Temp (C)
929.49
908.73
887.97
867.20
846.44
825.68
804.92
784.16
763.40
742.63
721.87
701.11
680.35
Matrix
Temp (C)
801.74
788.58
775.41
762.25
749.09
735.92
722.76
709.60
696.43
683.27
670.11
656.94
643.78
Ring

Fig. 20

Capsule	Compact OD (m)	Matrix ID (m)	Matrix OD (m)	Graphite Ring ID (m)	Graphite Ring OD (m)	Sink ID (m)	Sink OD (m)	Capsule ID (m)
1	0.01232	0.01246	0.02378	0.02451	0.03241	0.04003	0.06165	0.06476
2	0.01231	0.01246	0.02433	0.02451	0.03698	0.04003	0.06214	0.06476
3	0.01231	0.01246	0.02440	0.02451	0.03241	0.04003	0.06400	0.06476
4	0.01233	0.01246	0.02438	0.02451	0.03952	0.04003	0.06370	0.06476
5	0.01231	0.01246	0.02439	0.02451	0.03962	0.04003	0.06414	0.06476
6	0.01231	0.01246	0.02434	0.02451	0.03965	0.04003	0.06369	0.06476
7	0.01231	0.01246	0.02436	0.02451	0.03797	0.04003	0.06418	0.06476
8	0.01232	0.01246	0.02437	0.02451	0.03894	0.04003	0.06424	0.06476
9	0.01231	0.01246	0.02433	0.02451	0.03949	0.04003	0.06351	0.06476
10	0.01230	0.01246	0.02441	0.02451	0.03799	0.04003	0.06369	0.06476
11	0.01232	0.01246	0.02252	0.02451	0.03240	0.04003	0.06044	0.06476
12	0.01231	0.01246	0.02433	0.02451	0.03498	0.04003	0.06169	0.06476

Table 1

Capsule	Gap1 (m)	Gap2 (m)	Gap3 (m)	Gap4 (m)
1	6.858E-05	3.683E-04	3.810E-03	1.554E-03
2	7.620E-05	8.890E-05	1.527E-03	1.313E-03
3	7.620E-05	5.588E-05	3.813E-03	3.810E-04
4	6.350E-05	6.350E-05	2.565E-04	5.334E-04
5	7.366E-05	5.842E-05	2.032E-04	3.150E-04
6	7.620E-05	8.382E-05	1.905E-04	5.359E-04
7	7.620E-05	7.620E-05	1.029E-03	2.921E-04
8	6.858E-05	6.858E-05	5.461E-04	2.642E-04
9	7.620E-05	8.890E-05	2.692E-04	6.274E-04
10	8.128E-05	5.080E-05	1.024E-03	5.359E-04
11	6.858E-05	9.982E-04	3.818E-03	2.164E-03
12	7.620E-05	8.890E-05	2.527E-03	1.537E-03

Table 2

Radius change slopes for daily calculation ([Δr/r]_at EOI / FF_EOI), units are $(m^2/n) \times 10^{25}$							
Capsule	Compact	Inner ring ID	Inner ring OD	Outer ring ID	Outer ring OD	Sink ID	Sink OD
Capsule 01	-0.00398	0.00021	-0.00413	0.00050	-0.00044	0.00092	-0.00093
Capsule 02	-0.00347	0.00184	-0.00417	0.00231	-0.00234	-0.00589	-0.00079
Capsule 03	-0.00375	0.00324	-0.00377	0.00363	-0.00331	0.00174	-0.00163
Capsule 04	-0.00347	0.00346	-0.00454	0.00173	-0.00153	-0.00304	-0.00137
Capsule 05	-0.00347	0.00380	-0.00414	0.00142	-0.00128	-0.00258	-0.00164
Capsule 06	-0.00347	0.00392	-0.00417	0.00248	-0.00161	-0.00277	-0.00133
Capsule 07	-0.00370	0.00467	-0.00566	0.00346	-0.00328	-0.00253	-0.00165
Capsule 08	-0.00290	0.00264	-0.00275	0.00199	-0.00220	-0.00256	-0.00188
Capsule 09	-0.00347	0.00325	-0.00417	0.00242	-0.00141	-0.00344	-0.00138
Capsule 10	-0.00364	0.00241	-0.00403	0.00351	-0.00362	-0.00435	-0.00128
Capsule 11	-0.00347	0.00146	-0.00417	0.00228	-0.00261	not used	-0.00148
Capsule 12	-0.00343	0.00036	-0.00296	0.00009	0.00010	-0.01286	-0.00113
Capsule 11 Positive						0.00161	

Table 3